Full length article

Novel correlations between optical absorption and water desalination of Ag/Fe₃O₄ nanocomposite prepared by pulsed laser ablation in liquid

M. Nabil [a,*], S.S. Fouad [b], K. Easawi [a], S. Abdallah [a], Horia. F [a]

[a] *Department of Basic Engineering Sciences, Faculty of Engineering (Shoubra), Benha University, Cairo, Egypt*
[b] *Department of Physics, Faculty of Education, Ain Shams University, Cairo 11566, Egypt*

ARTICLE INFO

ABSTRACT

This work aimed to study the optical absorption and photo-thermal conversion efficiency by the addition of the surfactant (Triton X-100) to Ag/Fe₃O₄ Nanocomposites (NCs), prepared by using laser ablation technique. The nanoparticles were characterized by several techniques confirming the successfully prepared formation of the elemental composition and the average particle size. The Energy dispersive X-ray spectroscopy techniques (EDX) were helped in evaluating the compositional elemental ratio. The nano crystalline structure and morphology was investigated using X-ray diffraction (XRD) and the transmission electron microscope (TEM). The values of the optical absorption, thermal conductivity and photo-thermal conversion have been reported. A consistent linkage between energy gap (E_g), electronegativity $(\Delta\chi)$ and the refractive index (n), depending only on the absorbance spectrum of the samples, which was effectively enhanced with the introduction of Ag Nanoparticles (NPs) to Fe₃O₄ Nanocomposites. Several relations have been proposed for calculating the refractive index as function of (E_g) and $(\Delta\chi)$ values. Moreover, the electronic polarizability (α_e), the molar volume (V_m), molar refractive index (R_m), molar electronic polarizability (α_{me}) was calculated. The photo-thermal conversion results due to the addition of Ag NPs and the (Triton X-100), to Fe₃O₄ NPs, has been enhanced. The results imply a novel concept, of the effect of Nobel metal "Ag" on the magnetic nanoparticles, optical energy gap, optical conductivity, thermal diffusivity and thermal conductivity. Consequently, we can have an efficient way that can be used as a photo-thermal agent for water desalination.

1. Introduction

The global need for portable water requires sustainable approach for purifying alternative sources such as seawater evaporation. Fe₃O₄ NPs is consider a smart material because of its outstanding properties due to its small size, and high magnetism, low toxicity and its superior optical, electrical and thermal characteristics [1].

A great attention has been given to combine Fe₃O₄ Nanoparticles (NPs) with Nobel metals (NPs) such as Ag and Au [2–3]. These attempts were challenged by the unique properties included optical, biological properties and nanocomposite devices [4–5]. The silver NPs (Ag NPs) have been applied as a broad spectrum and highly effective bactericide. The silver -magnetic nanocomposite (NCs) can enhancement its photo-catalytic activity by decreasing the recombination of electron-hole pairs. The (Ag NPs) stand out in biomedical applications, especially as anti-tumorigenic and antibacterial agent also it is strongly absorb light in the visible region, because of the surface plasmon resonance (SPR) that is

highly dependent on NPs [6–8]. The large cross section absorption plasmonic NPs can generate a significant amount of heat that causes an increase in temperature in their vicinities.

The combination of Fe₃O₄ NPs and Ag NPs presents a promising strategy for targeted biomedical applications as both Nps reducing and capping agent, minimizing the nanomaterial toxicity. Many methods were used to prepare Ag/Fe₃O₄, such as thermal decomposition, co-precipitation, sol–gel method and laser ablation in liquid [3]. The properties of the prepared nanoparticles depend mainly on the method used for preparation.

Pulsed laser ablation technique is one of the most versatile and sustainable approach for the fabrication of nanostructure materials. This technique based on creating laser pulse trains inside any liquid medium [8–10].

This work aims to investigate the capability of adding Ag NPs to Fe₃O₄ NPs on modifying structural, morphological, optical properties, and thermal parameters. The influence of the addition of surfactant on

---

the efficiency of seawater has been evaluated. A detailed knowledge of the interrelation features between the optical parameters and the characterizations is of importance for improving the thermal efficiency of seawater desalination. The characterization of the nanocomposites has been done using EDX, TEM, XRD, and UV–vis absorption.

2. Experimental details

In this study we used a highly purity Ag metal plate (purity 99.99% from Sigma Aldric) with thickness of 2 mm, that used to prepared Ag NPs by using laser ablation technique, while the preparation of Fe_3O_4 magnetics nanoparticles (NPs) is prepared by Co-precipitation method was given in details in [11]. The silver nanoparticles used in the experimental work was obtained by laser ablation in distilled water. The beam of pulsed Q-Switched Nd:YAG (Quanta-Ray) laser with pulse duration of 8 ns, 1064 nm wavelength and repetition rate of 10 Hz were focused by a lens of focal length (f = 20 cm) on the surface of the silver target as shown in Fig. 1 (Step 1) [4–11]. The metal plate target was washed first using the ultrasonic bath for 30 min and cleaned with ethanol and distilled water and then fixed at 18 mm below the distilled water surface. The target of a thickness (2 mm) was fixed on the bottom of a vessel containing (20 ml) of distilled water. The powder form of Fe_3O_4 NPs was achieved, after being washed with acetone and dried in oven at 60–700 ^{0}C for 1 h as seen in Fig. 1 (Step 2) [11]. The Ag/Fe_3O_4 NCs was synthesized by mixing 1 mg of Ag nanoparticles, 5 mg of Fe_3O_4 NPs in 100 ml of DI water followed by sonication for 30 min as shown in Fig. 1 (Step 3).

The elemental composition of Fe_3O_4 NPs & Ag/Fe_3O_4 NCs were investigated by the Energy dispersive X-ray spectroscopy (EDX) (JOEL-JSM Model 5600). The particle size was identified by Transmission Electron microscope (HRTEM, JEOL JEM-2100 operated at 200KV with high resolution Gatan CCD bottom camera, Orius SC200). The phase and structure of the prepared samples were identified using grazing incident X-ray diffraction (GIXRD, Lab). The absorbance spectra of the nanocomposites were studied by UV–VIS spectrophotometry (V-670 Jasco double- beam spectrophotometer) at scanning wavelength from 800 to 200 nm. A quartz cuvette with a normal optical path length of 10 mm was used to perform the measurements. A highly sensitive (PA) (MTEC Model 300) was used for determining the thermal parameters. The solution temperature was monitored by using an optical fiber probe model (FOBS) immersed in the solution and connected to digital meter model (OMEGA-FOB). The registering of the change of temperature through time for the samples under study, was controlled by using a computer interface program.

3. Results and Discussions

3.1. EDX and elemental composition analysis

The particles, analysis of the microstructure of the performed compositions under study using the EDX from FESEM for Fe_3O_4 NPs and Ag/Fe_3O_4 NCs, are seen in Fig. 2(a) and (b). The strong Ag, Fe and O element peaks were observed in the EDX spectra, demonstrating the successful synthesis of the Fe_3O_4 NPs and Ag/Fe_3O_4 NCs and no other impurities were found in the samples. The strong peak appeared at 3 keV was the typically absorption signal of Ag owing to the strong surface plasmon resonance (SPR) [4].

3.2. Morphology and structures Ag NPs and Ag /Fe_3O_4 NCs

The surface properties of any sample, influence their optical properties which are important factor in any used applications. The comparison of the TEM images of Ag NPs and the particles of Fe_3O_4 NPs before and after the addition of Ag NPs are shown in Fig. 3 respectively. The Ag NPs were synthesized by laser ablation and their shape and size distribution were studied by transmission electron microscopy (TEM) as shown in Fig. 3 (a-d). The particle size of the synthesized Ag NPs shows that the size is nearly equal 10 nm [12,13].

In Fig. 3(e) the spherical morphology of Fe_3O_4 NPs nanoparticles image, can be observed as gray color. The distribution of the average particle size of Fe_3O_4NPs was about 20.8 nm as indicated in Fig. 3(f) and as presented in Table 1.The TEM images of the Ag/Fe_3O_4 NCs are illustrated in Fig. 3 (g-i),with an average particle size, about 30.8 nm as shown in Fig. 3 (j) and as presented in Table 1.

The X-ray diffraction patterns of Fe_3O_4 NPs, Ag NPs, and Ag/Fe_3O_4 NCs by using a varying diffraction angle from 10° to 90° are presented in Fig. 4. As seen, the appearance of diffraction peaks indicates that, the three samples have polycrystalline structure with orientation along with different planes. The characteristic diffraction peaks of the Fe_3O_4 NPs at 30^0, 35.1^0, 43.51^0, 55^0, 58^0 and the 63.06^0 Bragg angles are the diffractions of (220), (311) (400), (422), (511) and (440) lattice planes, respectively as seen in Fig. 4 (a). For Ag NPs the pattern clearly shows the main peaks at (2θ) 38.19^0, 44.37^0, 64.56^0, 77.47^0 and 83.44^0 corresponding to the (111), (200), (220), (311) and (331) planes, respectively as seen in Fig. 4 (b). By comparing JCPDS (file no: 89–3722), the typical pattern of green-synthesized Ag NPs is found to possess a face-centered cubic (fcc) structure [14].

The positions of the peaks of Ag/Fe_3O_4 NCs, unchanged compared with those of Fe_3O_4 NPs as seen in Fig. 4 (c). The average crystallite size was evaluated by the Debye–Scherrer formula [15]: -

$$D = \frac{0 \bullet 9\lambda}{B\cos\theta} \tag{1}$$

Where (β) is the full-width at half-maximum (FWHM) value of XRD
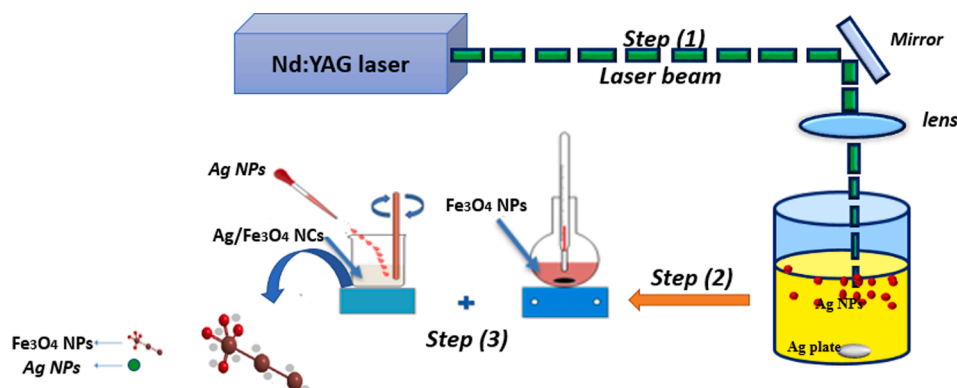
Fig. 1. Schematic illustration of the fabrication process of Ag/Fe3O4 Nanocomposite.
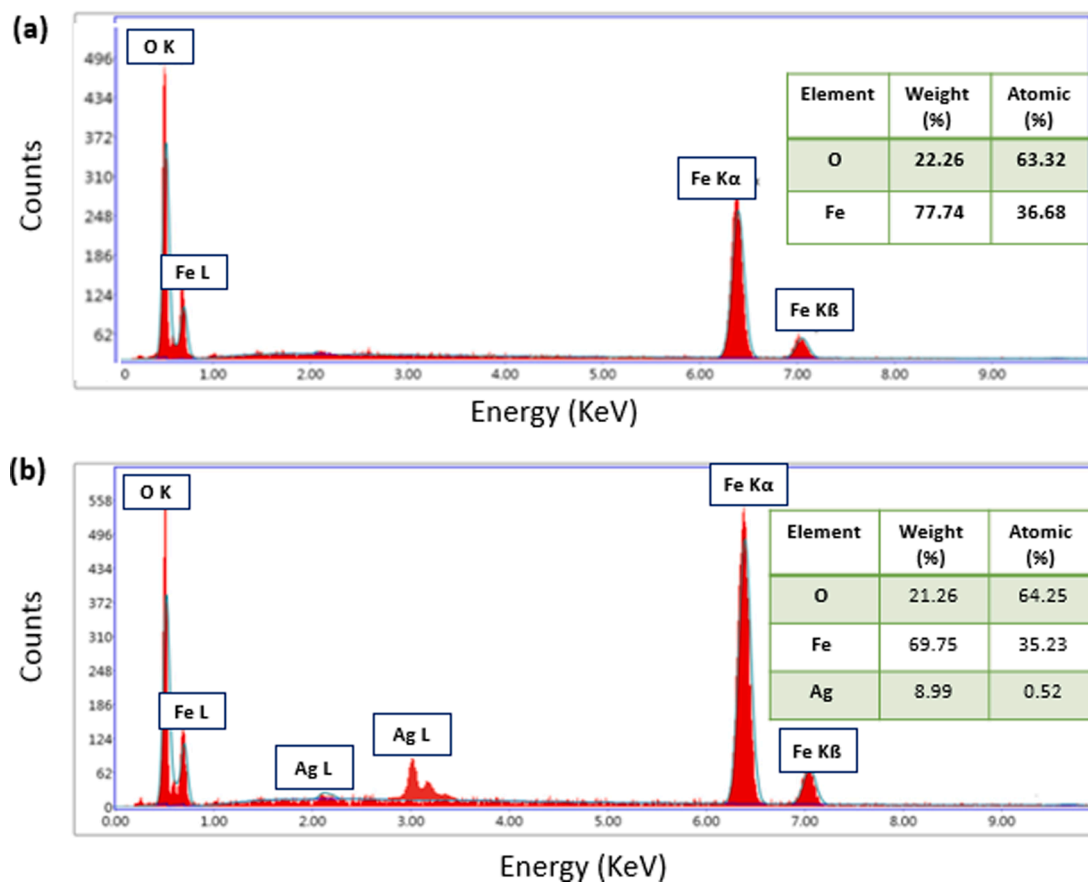
Fig. 2. EDX spectrum and the inset is weight percentage (wt.%) of Fe_3O_4 NPs and Ag/Fe_3O_4 NCs respectively seen in **(a)&(b).**
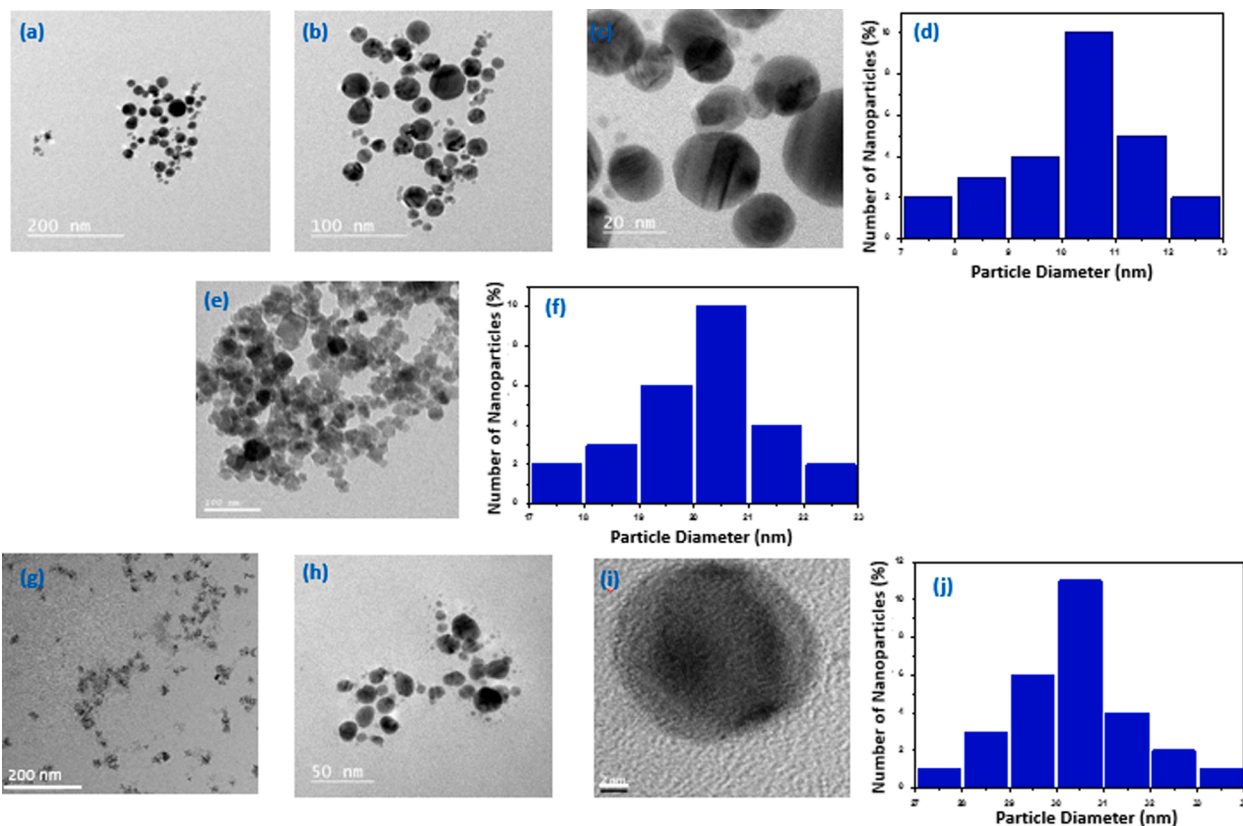
Fig. 3. TEM images with different magnification and particle size distribution (a-d) of Ag NPs, (e,f) of Fe_3O_4 NPs and (g-j) of Ag/Fe_3O_4 NCs respectively.

Table 1
The direct optical energy gap (E_g), the crystal size and the dislocation density (ρ) of Fe_3O_4 NPs and Ag/Fe_3O_4 NCs respectively.

Samples	Bandgap (E_g) (eV)	Size (nm)±0.01			$\rho(nm^{-2})$
		EMA	XRD	TEM	
Fe_3O_4 NPs	**1.57**	20.2	20.56	20	0.0025
Ag/Fe_3O_4 NCs	**1.35**	–	–	30.8	0.0010

diffraction lines, the wavelength $\lambda = 0.154056$ nm and (θ) is the half diffraction angle of (2θ). From TEM and XRD figures, we showed that the sizes are nearly the same as shown in Table 1. The dislocation density (ρ) is a measure of the number of dislocations in a unit volume of a crystalline materials. The dislocation density (ρ) = $1/D^2$ of Fe_3O_4 NPs and Ag/Fe_3O_4 NCs, is presented in Table 1 were (**D**) is the grain size. Large (**D**) and smaller (ρ) means better crystallization [16] as confirmed in Table 1.

3.3. The optical properties

The UV–Visible spectrum depends greatly on the particle size and the nature of the preparation as well. Fig. 5 **(a)** shows the variation of the Absorption of Ag NPs, Fe_3O_4 NPs and Ag/Fe_3O_4 NCs at different wavelength (200–800 nm).

For determining the accurate peak position of Ag, the second derivative analysis (SD) for NPs, Fe_3O_4 NPs and Ag/Fe_3O_4 NCs was used, as seen in Fig. 5**(b)**. The absorption peaks for Ag NPs in an aqueous solution is observed at 417 nm, and for Fe_3O_4 NPs at 385 nm. For Ag/Fe_3O_4 NCs, the absorption peak of Fe_3O_4 NPs is seen at 407 nm as seen in the inset of Fig. 5**(b)**. The observed small shift may be attributed to the charge transfer transition between the electrons of Ag NPs and Fe_3O_4 NPs, that causes a change in band gap energy between valance band and conduction band of Fe_3O_4 NPs and Ag/Fe_3O_4 NCs [17].

The particle size of Fe_3O_4 NPs can be defined from the absorption spectra by using the "Effective Mass Approximation" model (**EMA**) given by [18].

$$E_{gn} = E_{gb} + \frac{h^2}{8R^2}\left[\frac{1}{m_e} + \frac{1}{m_h}\right] - \frac{1.8e^2}{4\pi\varepsilon\varepsilon_0 R} \quad (2)$$

Where, E_{gn} is the electronic band gap for Nano crystals, E_{gb} is the band gap of bulk Fe_3O_4 (0.1 eV), **R** is the average radius of nanoparticles. m_e is the electron effective mass ($100m_o$), m_h is the hole effective mass ($100m_o$), $m_o = 9.11*10^{-31}$ Kg and ε is the dielectric constant for Fe_3O_4 sample [11]. The fraction of incident radiant energy which is absorbed per unit atom of an absorber called absorption coefficient (α) that provides information for determining the electronic transition and the band structure. The value of (α) was obtained from the expression given in details in [19].

Fig. 6**(a)** depicts the variation of absorption coefficient (α) for Fe_3O_4 NPs and Ag/Fe_3O_4 NCs versus the photon energy (**h υ**).

As seen the absorption coefficient (α) increases with the increases of the photon energy, and with the addition of Ag NPs to Fe_3O_4 NPs. The penetration depth or the skin depth (δ) is defined as the depth where the current density is about 37% of the value at the surface [20]. The skin depth (δ) is giving by the following relation ($\delta = 1/\alpha$). The dependence of the skin depth (δ) on photon energy is seen in Fig. 6 **(b)**. As can be seen the variation of (δ) is turned out to be due to the increase of the photon energy and the addition of Ag NPs to Fe_3O_4 NPs. Normally and according to the references the best fit obtained for the energy gap values (E_g) for the systems under study was for direct transition. The linear dependence of (αh υ)^2 on h υ using Tauc's equation is shown in Fig. 7.

The optical energy gap (E_g) can be determined on basis of equation [21]:

$$\alpha h\upsilon = A(h\upsilon - E_g)^r \quad (3)$$

where (**hυ**) is the incident photon energy, (**A**) is a constant, and (**r**) is an important factor that detects the type of existing transition. The best fit obtained for **r** = 1/2 as mentioned earlier for direct transition. Fig. 7 illustrates and confirm, the direct energy gap for Fe_3O_4 NPs and Ag/Fe_3O_4 NCs, and the band gap values were evaluated by extending the straight line of the curves to intercept the x-axis at zero (αh υ)^2. As can be seen the presence of Ag NPs affected the physical parameters, and band gap values decreases from 1.57 eV for Fe_3O_4 NPs to 1.35 eV for Ag/Fe_3O_4 NCs. The estimated values of the optical energy gap (E_g) are given in Table 1.

The observed decrease in the values of the energy gap against the addition of Ag NPs to Fe_3O_4 NPs can be attributed to the quantum size effect related to the particle size seen in Table 1. The correlation between the structural and optical properties suggests that the crystallite size is predominantly influenced by (E_g) [21]. The spacing of the electronic levels and the band gap decreases with increasing the particle size. The total electronegativity difference ($\Delta\chi$) can be obtained by substituting the value of (E_g) into the Duffy relation [22].

$$\Delta\chi = 0.2688 E_g \quad (4)$$

Different relations are presented between the refractive index (**n**) & (E_g) and ($\Delta\chi$) from the following relations [23–24].
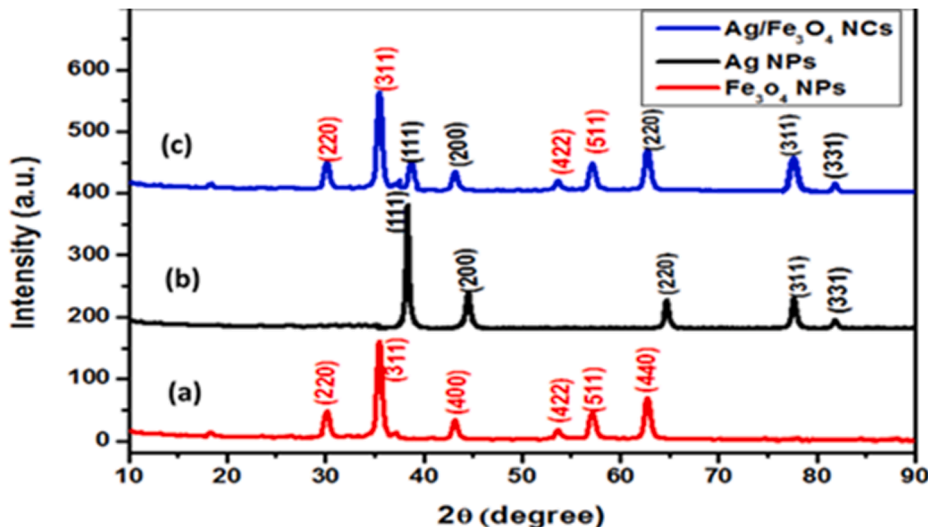
Fig. 4. Shows the XRD spectra of synthesized **(a)** Fe_3O_4 NPs, **(b)** Ag NPs and **(c)** Ag/Fe_3O_4 NCs respectively.

(a)

(b)
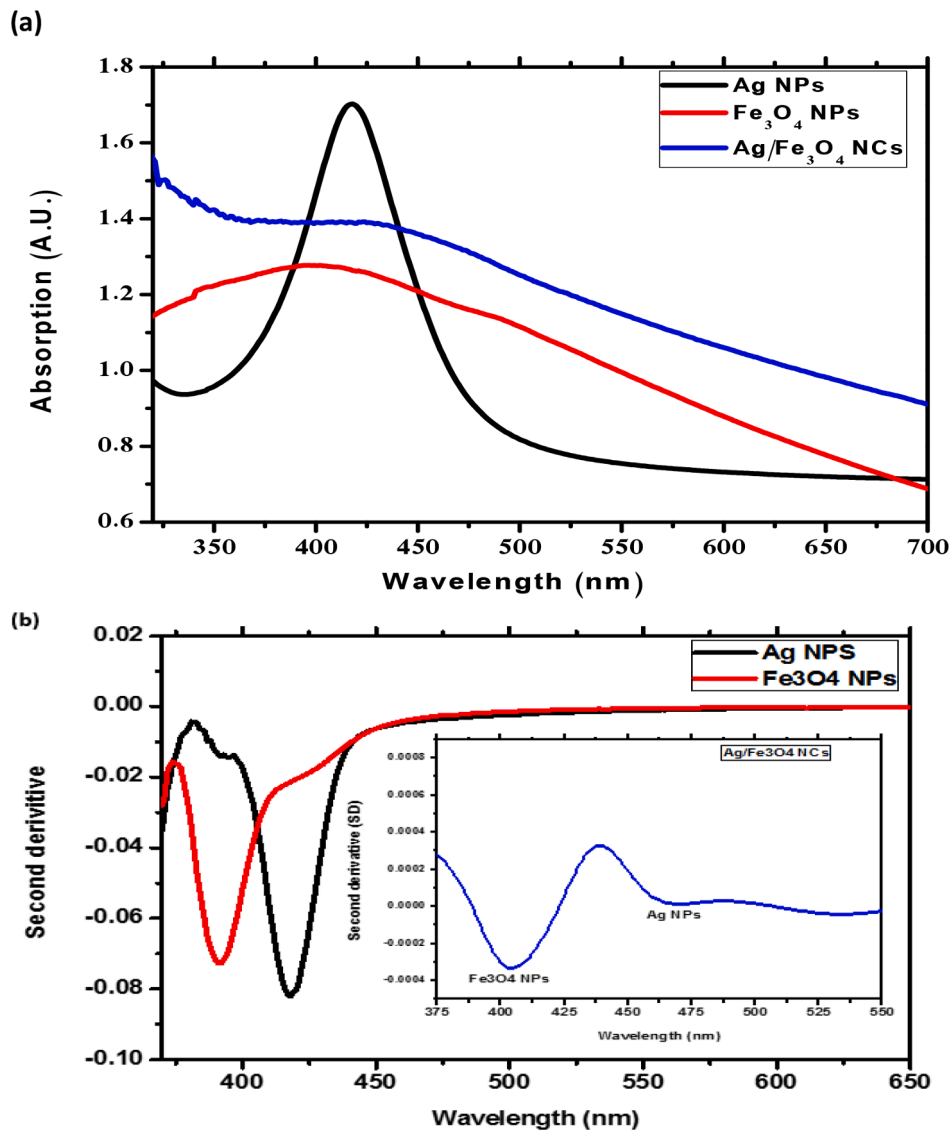
Fig. 5. (a) Absorption spectra of Ag NPs, Fe_3O_4 NPs and Ag/Fe_3O_4 NCs respectively. (b)The second derivative (SD) of Ag NPs and Fe_3O_4 NPs, the inset of Fig is the second derivative of Ag/Fe_3O_4 NCs.

(a)

(b)
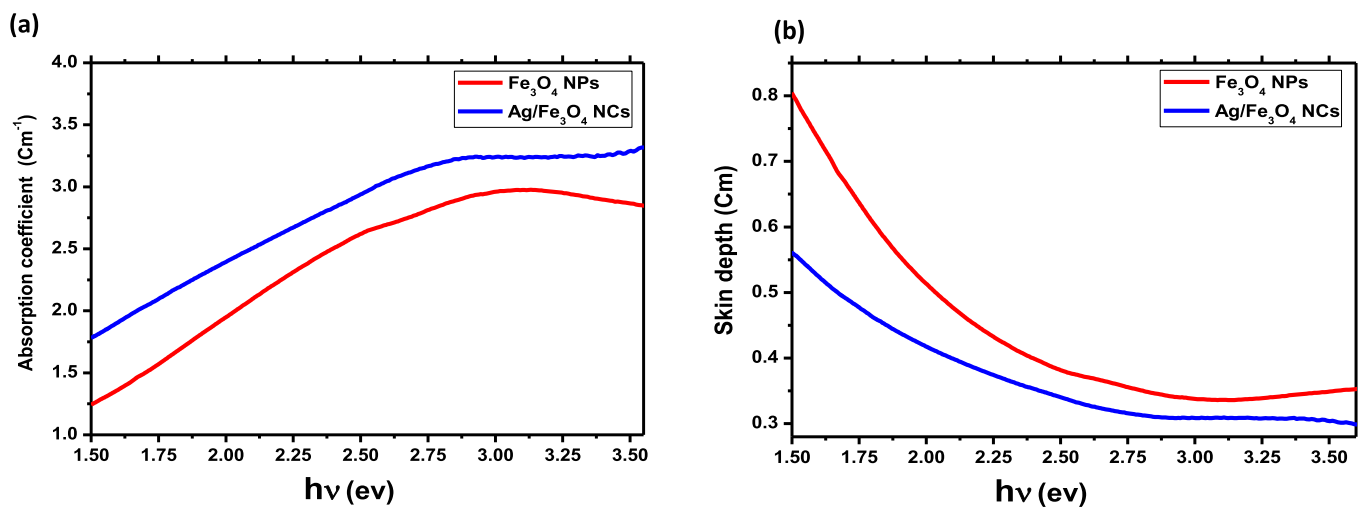
Fig. 6. (a) The absorption coefficient of Fe_3O_4 NPs and Ag/Fe_3O_4 NCs as a function of photon energy. (b) The skin depth of Fe_3O_4 NPs and Ag/Fe_3O_4 NCs as a function of photon energy.
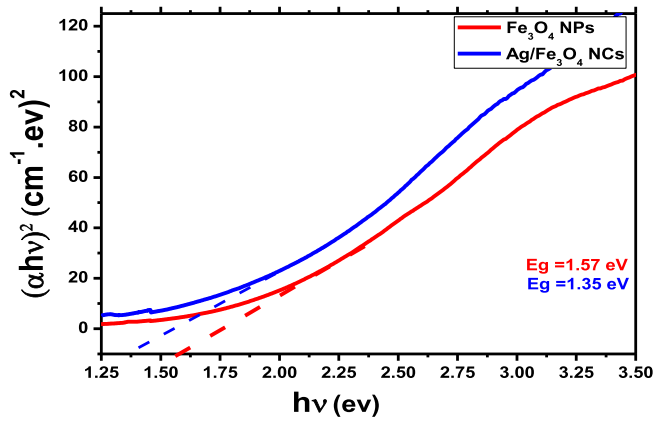
Fig. 7. ($\alpha h\nu^2$) versus (hν) for Fe3O4NPs and Ag/Fe$_3$O$_4$ NCs samples respectively.

$$n = -\ln(0.102\Delta\chi) \tag{5}$$

$$n = -\ln(0.027E_g) \tag{6}$$

The calculated values of refractive index (**n**) are presented in Table 2. The increase of the average refractive index (**n_{av}**) is an indication of the effect of Ag NPs on the optical property of Fe$_3$O$_4$ NPs. The wave velocity or the velocity of propagation (**v**) is the rate of speed that travels through a medium, the (**n_{av}**) is related to the velocity of propagation (**v**), and velocity of light (**c**) by (**$v = c/n$**) [25]. The calculated values of (**v**) for Fe$_3$O$_4$ NPs and Ag/Fe$_3$O$_4$ NCs are summarized in Table 2. The optical conductivity (**σ_{opt}**) is one of the important parameters that relate the absorption coefficient (**α**) with the refractive index (**n**). Moreover, the skin depth (**δ**) depends on the optical conductivity as well. The optical conductivity (**σ_{opt}**) is given by the following relation [26]:

$$\sigma_{opt} = \frac{\alpha n c}{4\pi} \tag{7}$$

The estimated values of the optical conductivity (**σ_{opt}**) have been presented in Fig. 8 as a function of photon energy. The figure reveals that, (**σ_{opt}**) increased by increasing the photon energy and the addition of the Ag NPs.

It is noted from the behavior of the skin depth (**δ**) presented in Fig. 6 (b) compared with that of the optical conductivity given in Fig. 8, that both figures, ensures the dependence of the conductivity on the skin depth "the higher optical conductivity (**σ_{opt}**) the smaller the skin depth (**δ**)".

The electronic polarizability can be evaluated by substituting the obtained value of (**n_{av}**) into this equation [27]:

$$\alpha_e = \frac{3(n_{av}^2 - 1)}{4\pi N_A (n_{av}^2 + 2)} \tag{8}$$

The molar volume (**V_m**) was calculated from the electronic polarizability (**α_e**) using the following relation [28]:

$$\alpha_e = 0.395(\frac{n_{av}^2 - 1}{n_{av}^2 + 1})V_m \tag{9}$$

The molar refraction (**R_m**) was calculated based on average refractive

Fig. 8. Optical conductivity (**σ_{opt}**) versus (**hν**) plot for Fe$_3$O$_4$ NPs and Ag/ Fe$_3$O$_4$ NCs respectively.

index and molar volume by using the relation [29]:

$$R_m = (\frac{n_{av}^2 - 1}{n_{av}^2 + 2})V_m \tag{10}$$

The molar electronic polarizability (**α_{me}**) is given by [30]:

$$\alpha_{me} = \frac{R_m}{2.52} \tag{11}$$

The calculated values of (**α_e**),(**V_m**), (**R_m**) and (**α_{me}**) are given in Table 3. As seen, the addition of Ag NPs to Fe$_3$O$_4$ NPs, leads to the increase in the electronic polarizability. The molar polarizability and the electronic polarizability relationship against the average refractive index and the molecular size are also confirmed. Since the electronic polarizability is closely related to many properties such as refraction, conductivity, absorption and molecule size "As the grain size or molecular size increases the polarizability also increases. The increase in the (**R_m**) value indicates clearly the dependence of (**R_m**) on the electronic polarizability. It is also noted that (**R_m**) increases as the (**V_m**) increases. This increase is accompanied by the increase of (**n_{av}**) since (**R_m**), must be calculated based on the refractive index deviation function,

3.4. Effect of the addition of Ag NPs on the desalination performance of Fe$_3$O$_4$ NPs

Desalination technology utilize thermal or electrical energy or both to separate water from salt. The feed water for desalination process can be seawater. The most widespread process for desalination depends on the energy source. The Photoacoustic (PA) technique was carried out for studying the thermal properties of the liquid form samples of Fe$_3$O$_4$ NPs and Ag/Fe$_3$O$_4$ NCs in seawater as seen in Fig. 9 **(a)**. The PA amplitude (**q**) and frequency (**f**) can be calculated from the well-known equation [31]:

$$q = \frac{A\beta\mu_s}{2\pi f e \sqrt{(\beta\mu_s + 1)^2 + 1}}, \quad \mu_s = \left(\frac{D_{th}}{\pi f}\right)^{\frac{1}{2}} \tag{12}$$

Table 2
The electronegativity (**$\Delta\chi$**), refractive index (**n**), velocity of propagation (**v**) of Fe$_3$O$_4$ NPs and Ag/Fe$_3$O$_4$ NCs respectively.

Samples	$\Delta\chi$	Equation (n)		Average (n) (n_{av})	v m/sec $\times 10^8$
		Eq (5)	**Eq (6)**		
Fe$_3$O$_4$ NPs	**0.422**	**3.14**	**3.16**	3.15	0.952
Ag/Fe$_3$O$_4$ NCs	0.362	3.29	3.31	3.30	0.909

Table 3
Electronic polarizability (**α_e**), molar volume (**v_m**), molar refraction (**R_m**) and molar electronic polarizability (**α_{me}**) of Fe$_3$O$_4$ NPs and Ag/Fe$_3$O$_4$ NCs respectively.

Samples	$\alpha_e \times 10^{-25}$	$V_m \times 10^{-25}$	$R_m \times 10^{-25}$	$\alpha_{me} \times 10^{-25}$
Fe$_3$O$_4$ NPs	**2.968**	**9.217**	**6.897**	**2.736**
Ag/Fe$_3$O$_4$ NCs	3.04	9.268	7.110	2.821
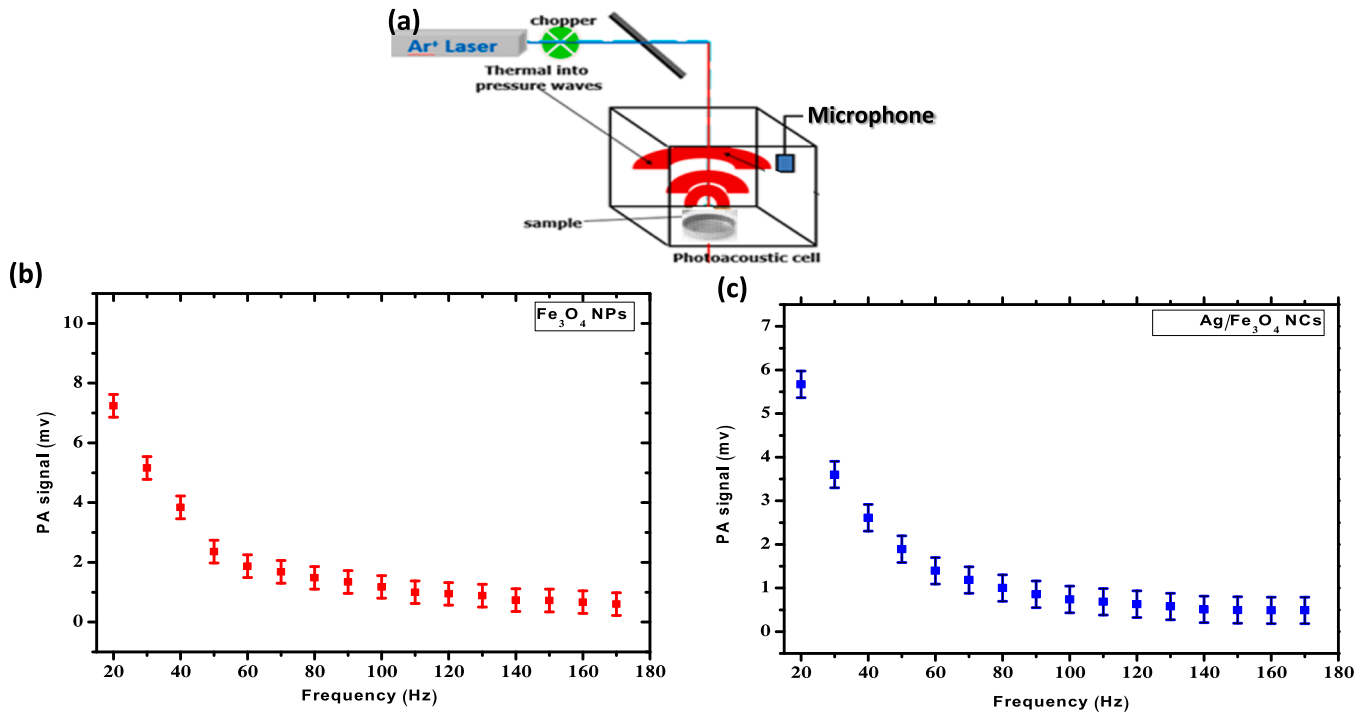
Fig. 9. (a) The experimental set-up (PA) diagram for thermal measurements. **(b), (c)** Relation of (**q**) versus (**f**) for Fe$_3$O$_4$ NPs and Ag/Fe$_3$O$_4$ NCs are respectively seen in.

Where (**β**) is the optical absorption coefficient, (**e**) is sample thermal effusivity, (**µ**$_s$) is thermal diffusion length and (**A**) is constant (not related to the sample). The desalination performance of Fe$_3$O$_4$ NPs and Ag/Fe$_3$O$_4$ NCs, was compared and displayed in Fig. 9 **(b)** and **(c)** for signal amplitude (**q**) versus (**f**). The fitting of Fig. 9 was utilized for determine the thermal diffusivity (**D$_{th}$**) and thermal effusivity (**e**) [32,33]. The value of the thermal conductivity (**k**) was given by the following equation:

$$K = e\sqrt{D_{th}} \tag{13}$$

The thermal conductivity (**K**) of Fe$_3$O$_4$ NPs value increased with the addition of Ag NPs in the Ag/Fe$_3$O$_4$ NCs Table 4, this may be due to the localized surface plasmon resonance. This results matched with the data of both the optical conductivity (**σ$_{opt}$**) and skin depth (**δ**) seen in Fig. 6**(b)** & Fig. 8. Heat transfer occurs with a lower rate for materials of low thermal conductivity than in material of high thermal conductivity. Therefore, the driving force of Fe$_3$O$_4$ NPs significantly strengthened by the addition of Ag NPs. In the current work, the water-based of Fe$_3$O$_4$ NPs and Ag/ Fe$_3$O$_4$ NCs were ultrasonically dispersed in seawater by using surfactant (Triton X-100) with concentration of 5 mg/5ml and 5 ml (NPs/water/surfactant respectively) [34]. The aim and the property of the used surfactant is given in details in [11].

The photo-thermal conversion characteristics of a solar NPs were investigated under solar simulator, xenon lamp with (200Watt and

Table 4
The three-thermal parameter of seawater, Fe$_3$O$_4$ NPs and Ag/Fe$_3$O$_4$ NCs respectively.

Sample	Thermal diffusivity (D$_{th}$) (Cm^2/s) × 10^{-7}	Thermal effusivity (e) (Ws$^{1/2}$Cm^{-2}K^{-1})	Thermal conductivity (k) (W/Cm.K)
Seawater	**1.380**	**0.158**	0.570
Fe$_3$O$_4$ NPs	**1.461**	**0.167**	0.603
Ag/Fe$_3$O$_4$ NCs	1.956	0.223	0.824

irradiance (1000 W/m^2) estimated by power meter at various duration time of (60) minutes as in Fig. 10 **(a)**. The increase of the temperature of the nanofluid than that of the base fluid (seawater) as shown in Fig. 10 **(b)**. The variation in the temperature is recommended that the strong absorption and the capturing of solar radiation that enhances the photo-thermal conversion efficiency, of Fe$_3$O$_4$ NPs and Ag/Fe$_3$O$_4$ NCs compared to base fluid.

3.5. Thermal efficiency on desalination performance

The thermal efficiency is a dimensionless performance that depends on overall loss coefficient which includes conduction, convection and radiation losses. In our case the temperature of the NPs is the same as the surrounding fluid, measured by the thermocouple, since the fluid depth is small and the solar radiation is uniform. The photo-thermal conversion efficiency (**η**) can be determined with the relation [35,36].

$$\eta = \frac{\Delta T c_w m_w}{\Delta t A G} \times 100\% \tag{14}$$

Where, (**c$_w$**) and (**m$_w$**) are the specific heat and the mass of the water, respectively, (**ΔT**) is the temperature difference of the nanofluid after an exposed time (**Δt**); (**A**) is the irradiation area; (**G**) (W m^{-2}) is the irradiation intensity. An increase in the efficiency by adding the surfactant (Triton X-100) to Fe$_3$O$_4$ NPs and Ag/Fe$_3$O$_4$ NCs is observed in Fig. 10 **(c),** were the presence of nanoparticle suspended in seawater increases the absorption (direct absorption) of incident radiation more than that of pure seawater, upon adding Ag NPs, which is an indication of the increase of heating efficiency. As we know the photo-thermal conversion is to convert sunlight into heat through the collection and absorption of the system, the volumetric absorption process addresses the limitation of the surface heat transfer process which is normally associated with the conversion efficiency. The presented absorption results indicate the linear relationship between absorbance and photo-thermal efficiency. This observation matched with the surface plasmons, as well as the increase of the absorption and thermal conductivity. Moreover a good agreement can be recognized when comparing the data of the average
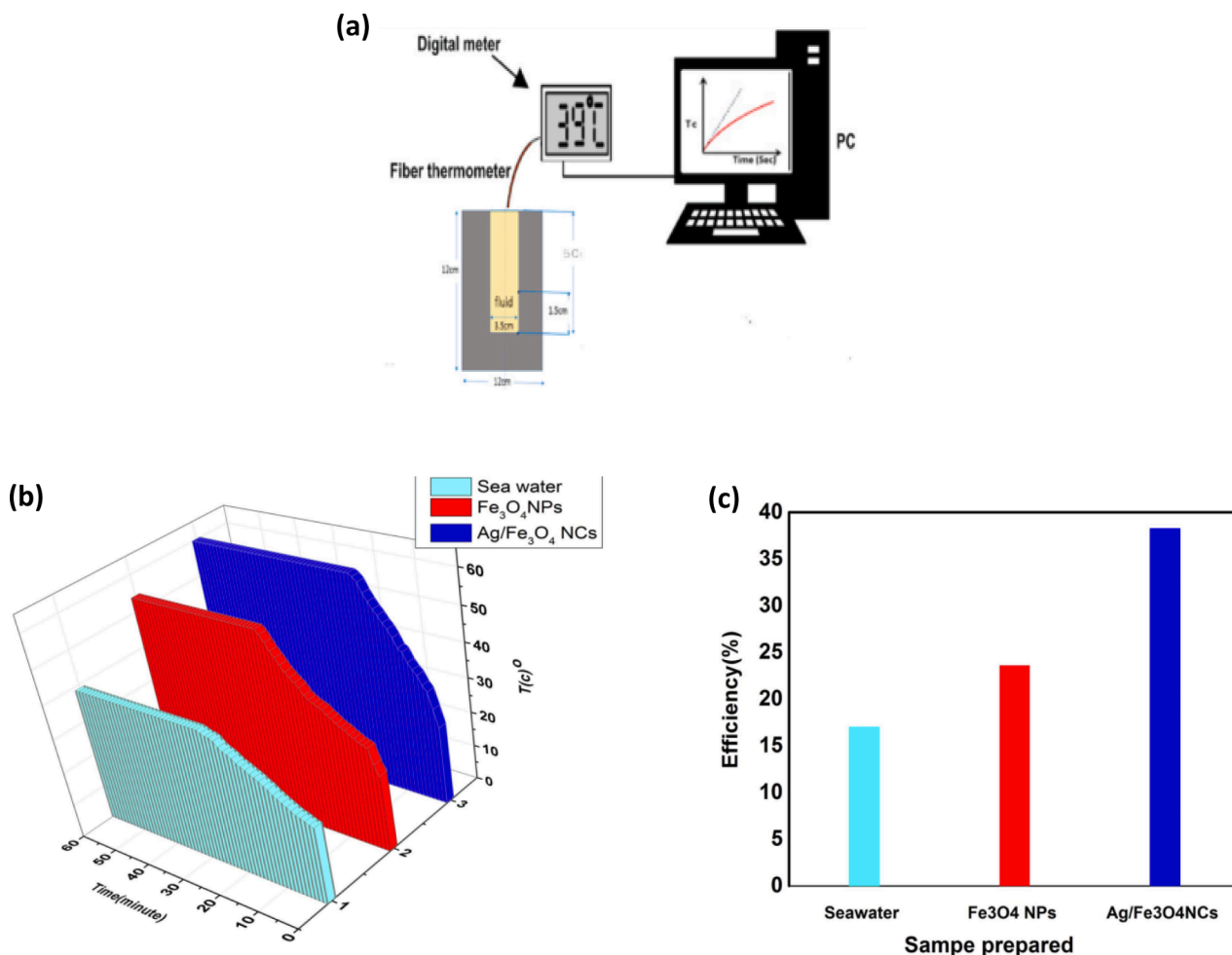
Fig. 10. (a) Experimental setup for registering the temperature rise with time. **(b)** The temperature distribution with time of Fe_3O_4 NPs, Ag/Fe_3O_4 NCs and seawater. **(c)** Photo-thermal conversion efficiency of Fe_3O_4 NPs, Ag/Fe_3O_4 NCs and seawater respectively.

refractive index (n_{av}) give in Table 2, with the given data presented in Table 4, were a higher temperature means the liquid becomes less dense causing light to travel faster in the medium.

4. Conclusion

The pulsed laser ablation was used to form the Ag/Fe_3O_4 NCs. The influence of Ag NPs on the optical and thermal properties of Fe_3O_4 NPs was systematically analyzed. The EDX, TEM, XRD studies showed that Fe_3O_4 NPs has polycrystalline structure and the composite particles had better responsive property with the addition of Ag NPs. The band-gap values (E_g) decreased from 1.57 to 1.35 eV and the refractive index (n) increased from 3.15 to 3.30 with the addition of Ag NPs to Fe_3O_4 NPs. From the optical energy gap, electronegativity ($\Delta\chi$) and refractive index (n) we calculated several parameters. In addition the values of the thermal diffusivity (D_{th}), thermal effectivity (e) and thermal conductivity (k) were determined.In regards to these characteristics, we can say that this work provides a simple and effective method for the detection of Ag/Fe_3O_4 NCs and the different obtained parameters could provide reference for solving the major problem of having unconventional water sources.

Auhtor Statement

M. Nabil:- The idea, Measured and calculated the different parameters and revision. **S.S. Fouad:-** Suggesting most of the calculated parameters and writting ,revising the hole text. **K. Easawi, S. Abdallah:-** Revision. **Horia.F:-** Prepared the samples, measured and revision.

Declaration of Competing Interest

The authors declare that they have no known competing financial interests or personal relationships that could have appeared to influence the work reported in this paper.

Data availability

No data was used for the research described in the article.

References

[1] Raid A. Ismail , Ghassan M. Sulaiman , Safa A. Abdulrahman , Thorria R. Marzoog, Anitbacterial activity of magnetic iron oxide nanoparticles synthesized by laser ablation in liquid. *Material Science and Enginering* C 53**(2015)**286-297.

[2] P. Miao, Y. Tang, L. Wang, DNA modified Fe_3O_4@ Au magnetic nanoparticles as selective probes for simultaneous detection of heavy metal ions, ACS Appl. Mater. Interfaces 9 (4) (2017) 3940–3947.

[3] Hassan H Bahjat, Raid A. Ismail, Ghassan M. Sulaiman, Synthesis and characterization of magnetite Fe3O4 nanoparticles using one step laser ablation in water under effect of external magnetic field. Journal of Physics : Conference series 1795**(2021)** 012028..

[4] M. Alheshibri, K. Elsayed, S.A. Haladu, S.M. Magami, A.A. Baroot, İ. Ercan, F. Ercan, et al., Synthesis of Ag nanoparticles-decorated on CNTs/TiO$_2$ nanocomposite as efficient photocatalysts via nanosecond pulsed laser ablation, Opt. Laser Technol. 155 (2022), 108443.

[5] X.-M. Li, X.u. Gaojie, Y. Liu, T. He, Magnetic Fe_3O_4 nanoparticles: Synthesis and application in water treatment, Nanoscience & Nanotechnology-Asia 1 (1) (2011) 14–24.

[6] Y. Cui, W. Hui, S.u. Jing, Y. Wang, C. Chen, Fe_3O_4/Au composite nano-particles and their optical properties, Sci. China, Ser. B 48 (4) (2005) 273–278.

[7] H. Aleali, L. Sarkhosh, M. Eslamifar, R. Karimzadeh, N. Mansour, Thermo-optical properties of colloids enhanced by gold nanoparticles, Jpn. J. Appl. Phys. 49 (8R) (2010), 085002.

[8] Gai, Ke, Huili Qi, Xiulan Zhu, and Mingye Wang. Preparation of Ag-Fe3O4 nanoparticles sensor and application in detection of methomyl. In *E3S Web of Conferences*, vol. 118, **(2019)** : 01002.

[9] D. Hao, S. Cheng-Min, X.u. Hui Chao, L.C. Zhi-Chuan, T. Yuan, S. Xue-Zhao, G. Hong-Jun, Synthesis and properties of Au–Fe3O4 and Ag–Fe3O4 heterodimeric nanoparticles, Chin. Phys. B 19 (6) (2010), 066102.

[10] K. Easawi, M. Nabil, T. Abdallah, S. Negm, H. Talaat, Plasmonic absorption enhancement in Au/CdS nanocomposite, World Acad. Sci. Eng. Technol. 6 (2012) 25.

[11] M. Nabil, F. Horia, S.S. Fouad, S. Negm, Impact of Au nanoparticles on the thermophysicalparameters of Fe3O4 nanoparticles for seawater desalination, Opt. Mater. 128 (2022), 112456.

[12] A. Radoń, A. Drygała, Ł. Hawełek, D. Łukowiec, Structure and optical properties of Fe3O4 nanoparticles synthesized by co-precipitation method with different organic modifiers, Mater Charact 131 (2017) 148–156.

[13] H.R. Shahverdi, M. Shakibaie, K.M. Moghaddam, M. Amini, H. Montazeri, A. R. Shahverdi, Semi-biosynthesis of magnetite-gold composite nanoparticles using an ethanol extract of Eucalyptus camaldulensis and study of the surface chemistry, J. Nanomater. (2009).

[14] H. Salehizadeh, E. Hekmatian, M. Sadeghi, K. Kennedy, Synthesis and characterization of core-shell Fe3O4-gold-chitosan nanostructure, J. Nanobiotechnol. 10 (1) (2012) 1–7.

[15] D. Padiyan, A.M. Pathinettam, K.R. Murali, Influence of thickness and substrate temperature on electrical and photoelectrical properties of vacuum-deposited CdSe thin films, Mater. Chem. Phys. 78 (1) (2003) 51–58.

[16] S.S. Fouad, M. Bence Parditka, E.B. Nabil, S. Negm, Z. Erdélyi, "Effect of Cu Interlayer on Opto-Electrical Parameters of Zno Thin Films, J Mater Sci: Mater Electron 33 (2022) 20594–20603.

[17] Jannah, N. R., and D. Onggo. Synthesis of Fe3O4 nanoparticles for colour removal of printing ink solution. In *Journal of Physics: Conference Series*, vol. 1245, no. 1, p. 012040. IOP Publishing, **(2019)**.

[18] M. Nabil, S.A. Mohamed, K. Easawi, S.SA. Obayya, S. Negm, H. Talaat, M.K. El-Mansy, Surface modification of CdSe nanocrystals: Application to polymer solar cell, Curr. Appl Phys. 20 (3) (2020) 470–476.

[19] S.S. Fouad, B. Parditka, M. Nabil, E. Baradács, S. Negm, H.E. Atyia, Z. Erdélyi, Bilayer number driven changes in polarizability and optical property in ZnO/TiO2 nanocomposite films prepared by ALD, Optik 233 (2021) 166617.

[20] J. Tauc, R.d. Grigorovici, A. Vancu, Optical properties and electronic structure of amorphous germanium, physica status solidi (b) 15 (2) (1966) 627–637.

[21] S.S. Fouad, B. Parditka, A.E. Bekheet, H.E. Atyia, Z. Erdélyi, ALD of TiO2/ZnO mutilayers towards the understanding of optical properties and polarizability, Opt. Laser Technol. 140 (2021), 107035.

[22] J.A. Duffy, Trends in energy gaps of binary compounds: an approach based upon electron transfer parameters from optical spectroscopy, J. Phys. C Solid State Phys. 13 (16) (1980) 2979.

[23] R.R. Reddy, Y. Nazeer Ahammed, K. Rama Gopal, P. Abdul Azeem, T.V.R. Rao, P. Mallikarjuna Reddy, Optical electronegativity, bulk modulus and electronic polarizability of materials, Opt. Mater. 14 (4) (2000) 355–358.

[24] T.S. Moss, Relations between the refractive index and energy gap of semiconductors, physica status solidi (b) 131 (2) (1985) 415–427.

[25] I.M. El Radaf, H.Y.S. Al-Zahrani, S.S. Fouad, M.S. El-Bana, Profound optical analysis for novel amorphous Cu2FeSnS4 thin films as an absorber layer for thin film solar cells, Ceram. Int. 46 (11) (2020) 18778–18784.

[26] S. S. Fouad,.I. M. El Radaf, Pankaj Sharma, and M. S. El-Bana. Multifunctional CZTS thin films: structural, optoelectrical, electrical and photovoltaic properties. Journal of Alloys and Compounds 757 **(2018):** 124-133.

[27] S.A. Umar, M.K. Halimah, K.T. Chan, A.A. Latif, Polarizability, optical basicity and electric susceptibility of Er3+ doped silicate borotellurite glasses, J. Non Cryst. Solids 471 (2017) 101–109.

[28] Hanaa. Zaka,, B. Parditka, Z. Erdélyi, H. E. Atyia, Pankaj Sharma, and S. S. Fouad. Investigation of dispersion parameters, dielectric properties and opto–electrical parameters of ZnO thin film grown by ALD. Optik 203 **(2020):** 163933.

[29] Abdel-Basset, Dalia M., Suresh Mulmi, Mohammed S. El-Bana, Suzan S. Fouad, and Venkataraman Thangadurai. "Structure, Ionic Conductivity, and Dielectric Properties of Li-Rich Garnet-type Li5+ 2 x La3Ta2−x Sm x O12 (0≤ x≤ 0.55) and Their Chemical Stability." *Inorganic chemistry* 56, no. 15 (2017): 8865-8877.

[30] M.K. Halimah, A.A. Awshah, A.M. Hamza, K.T. Chan, S.A. Umar, S.H. Alazoumi, Effect of neodymium nanoparticles on optical properties of zinc tellurite glass system, J. Mater. Sci. Mater. Electron. 31 (5) (2020) 3785–3794.

[31] P. Poulet, J. Chambron, R. Unterreiner, Quantitative photoacoustic spectroscopy applied to thermally thick samples, J. Appl. Phys. 51 (3) (1980) 1738–1742B.

[32] W. Aldama-Reyna, J.F. Agreda-Delgado, M.A. Valverde-Alva, L.M. Angelats-Silva, Photoacoustic study of Changes in Optical Properties of Colloids with Silver Nanoparticles Produced by Laser Ablation, Int. J. Appl. Eng. Res. 13 (2) (2018) 1408–1414.

[33] Horia, F., Khaled Easawi, Reda Khalil, Said Abdallah, Mabrouk El-Mansy, and Sohair Negm. Optical and Thermophysical Characterization of Fe3O4 nanoparticle. *In IOP Conference Series: Materials Science and Engineering,* vol. 956, no. 1, p. 012016. IOP Publishing, **(2020)**.

[34] Y. Yung-Jih, D.S. Corti, E.I. Franses, Effect of Triton X-100 on the stability of titania nanoparticles against agglomeration and sedimentation: A masked depletion interaction, Colloids Surf A Physicochem Eng Asp 516 (2017) 296–304.

[35] M.W. Shahzad, M. Burhan, D. Ybyraiymkul, K.C. Ng, Desalination processes' efficiency and future roadmap, Entropy 21 (1) (2019) 84.

[36] H. Zhang, H.-J. Chen, D.u. Xiaoze, D. Wen, Photothermal conversion characteristics of gold nanoparticle dispersions, Sol. Energy 100 (2014) 141–147.